Science and Technology of Advanced Materials

ISSN: (Print) (Online) Journal homepage: www.tandfonline.com/journals/tsta20

Effect of P doped bimetallic FeCo catalysts on carbon matrix for oxygen reduction in alkaline media

Yuqi Ma & Hyo-Jin Ahn

To cite this article: Yuqi Ma & Hyo-Jin Ahn (03 Feb 2025): Effect of P doped bimetallic FeCo catalysts on carbon matrix for oxygen reduction in alkaline media, Science and Technology of Advanced Materials, DOI: 10.1080/14686996.2025.2459051

To link to this article: https://doi.org/10.1080/14686996.2025.2459051

© 2025 The Author(s). Published by National Institute for Materials Science in partnership with Taylor & Francis Group.

View supplementary material

Accepted author version posted online: 03 Feb 2025.

Submit your article to this journal

View related articles

View Crossmark data

Full Terms & Conditions of access and use can be found at
https://www.tandfonline.com/action/journalInformation?journalCode=tsta20

Check for updates

Publisher: Taylor & Francis & The Author(s). Published by National Institute for Materials Science in partnership with Taylor & Francis Group.

Journal: *Science and Technology of Advanced Materials*

DOI: 10.1080/14686996.2025.2459051

Effect of P doped bimetallic FeCo catalysts on carbon matrix for oxygen reduction in alkaline media

Yuqi Ma, and Hyo-Jin Ahn*

Department of Materials Science and Engineering, Seoul National University of Science and Technology, Seoul 01811, Korea

*Corresponding author Tel.: +82-2-970-6622

Email address: hjahn@seoultech.ac.kr (H.-J. Ahn)

yqma@seoultech.ac.kr (Yuqi Ma)

ACCEPTED MANUSCRIPT

Effect of P doped bimetallic FeCo catalysts on carbon matrix for oxygen reduction in alkaline media

Abstract

Catalysts' redox reactions are crucial for storage and energy conversion. Therefore, the fabrication of cost-effective, structurally rational, and multifunctional advanced catalytic materials continues to be a crucial task. In this study, we obtained P, Fe, and Co co-doped, nitrogen-rich carbon nanofibers by directly forming carbon nanotubes from metal-organic frameworks through electrospinning and pyrolysis. The $P_{0.025}$-FeCo/C catalyst demonstrated outstanding ORR activity, including an ECSA of 1954.3 cm², a limited current density of -3.98 mA/cm^2, an $E_{1/2}$ of ~ 0.84 V, and an E_{onset} of ~ 0.94 V. After 5000 cycles, the $P_{0.025}$-FeCo/C catalyst demonstrated remarkable enduring stability. These function enhancements occurred because of the electronic coupling between the metal and phosphorus, which altered the electron distribution at the metal center and optimized its electronic structure, thereby improving catalytic activity and stability. It exhibits good chemical stability in alkaline media and can maintain its catalytic performance for a long time, demonstrating good durability. Its tubular structure provides many active sites and superior electron transport paths owing to its unique channels and cavities, which help improve its activity and stability. Therefore, $P_{0.025}$-FeCo/C is expected to become a non-precious metal catalyst for facilitating oxygen reduction reactions.

Keywords: Metal-organic framework; oxygen reduction reactions; P doping, transition metal phosphides; carbon nanotubes

ACCEPTED MANUSCRIPT

1. Introduction

Amidst globalization and industrialization, environmental pollution has become a significant challenge for human civilization. The extensive widespread burning of fossil fuels has led to global climate change and a decline in air quality, posing threats to biodiversity and ecological balance and significantly jeopardizing human health and economic developments. To mitigate this trend, new energy technologies are being

sought to replace traditional fossil fuels [1-5]. Fuel cells and metal-air batteries are considered strong candidates for future energy sources due to their renewability, cleanliness, and high energy density [6-7]. Oxygen reduction reactions (ORR) are crucial cathodic reactions in metal-air batteries and fuel cells. Despite this, the sluggish kinetics of the ORR has long been a significant challenge, necessitating high activity and durable electrocatalysts. Although precious metal catalysts like platinum and palladium demonstrate specific catalytic properties, poor stability; their high cost, and scarcity, limit their extensive application. Researchers have developed and applied transition metal catalysts to address these shortcomings. Transition metals, like nickel, cobalt, iron, and copper, have emerged as ideal alternatives to noble metal catalysts owing to their abundant reserves, excellent electrochemical properties, and low cost [8-10]. Through rational structural design, crystal morphology control, and surface modification, the ORR capabilities of transition metal catalysts can be significantly optimized to meet the high efficiency, long life, and cost-effective demands of battery technology [11-14]. Among the various transition metal electrocatalysts explored, transition metal phosphides (TMPs), a class of interstitial compounds, have garnered significant interest due to their high catalytic performance, multifunctionality, and electrochemical stability [15-16]. The unique electronic structure and suitable electron density of TMPs provide excellent electrocatalytic properties [17-18]. Moreover, they have good chemical and electrochemical stability in alkaline environments, and they do not dissolve or structurally collapse easily. Furthermore, their strength does not decrease during long-term use [19]. Therefore, they have broad application prospects in energy conversion and storage.

Electrospinning is a processing method that yields ultrafine polymer fibers with multiple functions by forming a jet from a charged polymer solution or melting in an

ACCEPTED MANUSCRIPT

electrostatic field [20]. Electrospun materials have shown great potential for energy storage and transformation due to their good composition and structural control, exceptional mechanical strength, and flexibility [21]. Metal-organic framework (MOF) has been extensively investigated as promising catalyst supports because of their physical characteristics and distinctive chemical, particularly their highly tunable pore sizes, exceptional chemical functionalities, controllable crystal morphologies, and high surface areas [22-24]. MOFs have regular hexagonal or polyhedral shapes. Among the many structures of MOFs, tubular structures provide many active sites and superior electron transfer paths owing to their unique channels and cavities. Therefore, a tubular structure is an effective catalyst design. This structure enhances catalyst's activity and stability while also promotes the diffusion and adsorption of reactant molecules, further improving the catalytic efficiency [25-28]. However, MOFs may suffer structural damage or oxidation in aqueous solutions and oxygen environments, resulting in an unstable catalytic performance [29-31]. Combining electrospinning with MOF to prepare porous carbon nanofibers (CNFs), which can effectively adjust the porosity and mechanical strength of the composite material, provide abundant active sites, and promote oxygen reduction reactions [32-34]. However, the prepared nanofiber catalysts have limitations that hinder their further application. Zhang et al. successfully prepared a nanofiber membrane loaded with HKUST-1 (one of the extensively researched MOFs) by electrospinning HKUST-1 particles. The membrane exhibited excellent catalytic performance because of its rough single-fiber structure. However, the size of the HKUST-1 particles limited their application [35]. Li et al. synthesized a new $NiCo_2S_4$/CNFs composite material using electrospinning and hydrothermal methods, which ensured adequate edge exposure of the material to enhance electron diffusion and transport in the nanoparticles [36]. However, hydrothermal methods increase the cost

ACCEPTED MANUSCRIPT

and time required for experiments. Polymer nanofiber membranes must be immersed in a precursor solution, and controlling the nucleation and growth stages of crystals is challenging. Therefore, catalytic materials with a simple preparation process, high electrocatalytic activity, and stable products need to be studied and developed as effective ORR electrocatalysts.

This study introduces a facile strategy for preparing P, Fe, and Co co-doped carbon matrix (P-FeCo/C) catalysts via electrospinning. During the fabrication, poly (methyl methacrylate) (PMMA) was employed as a template polymer to obtain porous CNFs via high-temperature pyrolysis. Carbon nanotubes grew directionally around CNF from the MOFs, and the porous structure offered additional space for their formation. Subsequently, the synthesized P-FeCo/C was evaluated as an ORR catalyst. The prepared carbon nanotubes had resilient frameworks, and large specific surface areas, thereby exhibiting good mechanical stability, fast mass transfer, and high electrochemical performance. Furthermore, electronic regulation promoted by P, Fe, and Co co-doping significantly enhanced the electrochemical stability and catalytic performance of carbon supports. The prepared P-FeCo/C catalyst demonstrated outstanding ORR catalytic performance in alkaline electrolytes. This study opens a new direction for advancing efficient non-noble metal catalysts for metal-air batteries and fuel cells based on MOFs.

ACCEPTED MANUSCRIPT

2. Experimental

Iron (III) chloride hexahydrate, cobalt (II) nitrate hexahydrate, polyacrylonitrile (PAN), poly (methyl methacrylate), N, N-dimethylformamide (DMF), 2-methylimidazole (MIM), methanol, potassium hydroxide, phosphoric acid, 2-propanol, and a Nafion® perfluorinated resin solution were acquired from Sigma-Aldrich. Platinum, nominally 20% on carbon black, HiSPEG 3000 (Pt/C) was acquired from Thermo Scientific

Chemicals. Water purified with a Milli-Q purifier (IQ 7003; Millipore Co., USA) was utilized in all experiments. All reagents were used without further purification.

P, Fe, and Co co-doped CNFs were successfully synthesized via electrospinning, in situ growth, and pyrolysis. PAN (1 g), PMMA (1 g), MIM (0.3 g), and phosphoric acid (0.01, 0.015, 0.025, or 0.03 wt. %) were dissolved in DMF (11 mL) with constant stirring for 6 h to obtain a uniform electrospinning solution. The applied needle distance, flow rate, and voltage were 15 cm, 0.06 mL h^{-1}, and 16 kV, respectively. A membrane was collected after 12 h, and it was denoted as P/MIM/PAN/PMMA. Subsequently, iron (III) chloride hexahydrate (0.27 g) and cobalt (II) nitrate hexahydrate (0.29 g) were completely mixed into methanol (20 mL). Following this, the composite membrane (0.5 g) was directly submerged in the prepared solution and allowed to react for 12 h. The obtained composite membrane was denoted as P/MOF/PAN/PMMA. Finally, the P/MOF/PAN/PMMA composite membrane was stabilized for 2.5 h at 280 °C in air and then heat-treated in nitrogen for 2 h at 800 °C. The collected samples were designated as P_X-FeCo/C (where X denotes the phosphoric acid weight ratio = 0.01, 0.015, 0.025, or 0.03). FeCo/C: The preparation method was the same as $P_{0.025}$-FeCo/C, but phosphoric acid was not added to prepare the electrospinning solution. $P_{0.025}$-Co/C: The preparation method was the same as $P_{0.025}$-FeCo/C; iron chloride hexahydrate was not added during the experiment. $P_{0.025}$-Fe/C: The preparation method was the same as $P_{0.025}$-FeCo/C; cobalt nitrate hexahydrate was not added during the experiment.

The elemental distribution and morphology of the synthesized samples were examined using energy-dispersive spectroscopy (EDS; JEOL, NEO ARM) mapping and field-emission scanning electron microscopy (FESEM; EVO10, Carl Zeiss). The crystal structure, chemical bonding configurations, and surface functional characteristics of the samples were investigated by Raman spectroscopy (JASCO NRS-5100), X-ray

ACCEPTED MANUSCRIPT

diffraction (XRD; Rigaku D/Max-2500 diffractometer with Cu Kα radiation in the 2 theta range from 10 to 90° with a step size of 0.02°at a 40 kV and 40 mA), and X-ray photoelectron spectroscopy measurements (XPS, ESCALAB 250 equipped with an Al Kα X-ray source (hν = 1486.6 eV), the vacuum of the analysis chamber was $8 \times l0^{-10}$ Pa, the operating voltage was 12.5 kV, the filament current was 16 mA. The binding energies of target elements were calculated using a pass energy of 29.3 eV and a precision of roughly 0.3 eV), respectively.

Electrochemical evaluations were conducted using a galvanostat/potentiostat (Ecochemie Autolab) and 0.1 M KOH electrolyte. A three-electrode system is composed of a working electrode (glassy carbon), a counter electrode, and a reference electrode (Ag/AgCl) (sat. KCl). This potentiostat/galvanostat had an electrochemical workstation and a rotating disc electrode featuring a speed regulator. The prepared sample was used as a catalyst (0.01 g). It was dissolved in a mixture of 2-propanol (900 μL), deionized water (50 μL), and Nafion® perfluoro resin solution (57.4 μL) and stirred for 12 h to achieve a uniform ink. Cyclic voltammetry (CV) was conducted under O_2- and Ar- saturated conditions. Linear sweep voltammetry (LSV) was performed in an O_2-saturated environment at a scan rate of 5 mV/s. Finally, an accelerated durability test (ADT) was performed over 5000 cycles at a scanning rate of 100 mV/s to verify the sustained electrocatalytic performance. After completion of the ADT, the LSV analyses were conducted again at 1600 rpm.

3. Results and discussion

As shown in Figure 1, P, Fe, and Co co-doped CNFs were successfully synthesized via electrospinning, in situ growth, and pyrolysis. During the fabrication, PMMA was employed as a template polymer to obtain porous CNFs via high-temperature pyrolysis. Carbon nanotubes grew directionally around CNF from the MOFs, and the porous

ACCEPTED MANUSCRIPT

structure offered additional space for their formation. The prepared P-FeCo/C catalyst demonstrated outstanding ORR catalytic performance in alkaline electrolytes.

As depicted in Figures 2 (a–h), the microstructure and morphology of the samples annealed at 800 °C were examined by FESEM. As shown in Figure 2 (a, e), $P_{0.01}$-FeCo/C exhibited uniform, densely packed hair-like nanotube growth on the carbonized fibers. The diameters of the carbonized fibers and hair-like nanotubes were approximately 650 and 280 nm, respectively. In Figures 2 (b, f and c, g), nanotubes with gradually decreasing densities can be observed on the carbon fibers of $P_{0.015}$-FeCo/C and $P_{0.025}$-FeCo/C. Furthermore, no nanotubes were observed on the $P_{0.03}$-FeCo/C (Figure 2 (d, h)) CNFs, and irregular polygonal granular structures appeared. This was attributed to excess phosphoric acid, which caused phosphates to form new coordination complexes with metal ions [37].

Figure 3 (a) shows carbon nanotubes with a diameter of about 220 nm in the carbon matrix, and particles sized approximately 160 nm in the carbon nanotubes. Magnify the nanotubes using high-resolution transmission electron microscopy (HR-TEM). The bright area of a lattice edge space, representing the plane of graphite (002), was approximately 0.34 nm. In addition, the lattice fringes corresponding to the (210) and (111) planes of iron phosphide and cobalt phosphide were observed at approximately 0.20 nm and 0.25nm, respectively (Figure 3 (b)). During heat treatment, the coordination bonds linking the organic ligands with metal ions are severed, and the metal ions capture P ions to form metal phosphides (MPs) nanoparticles. Organic residues are catalyzed into carbon nanotubes on nanocatalysts. TEM-EDS mapping was performed on $P_{0.025}$-FeCo/C to verify its elemental distribution. Figure 3 (c) illustrates that N and C were evenly distributed in the carbon matrix, whereas Fe, Co, and P were more localized along the MP nanoparticles. Moreover, large amounts of N, Fe, Co, and

ACCEPTED MANUSCRIPT

P were similarly distributed throughout the carbon matrix, leading to heavy heteroatom doping of the carbon matrix, which can destroy the integrity of π-conjugated structures and induce defects.

The XRD pattern in Figure 4 (a) shows the sample's crystal structure. All samples displayed a broad diffraction peak at approximately 25.7°, attributed to the graphite (002) plane (JCPDS 65-6212) [38], with sharp peaks of diffraction at 44.7, 65.0 and 82.3, which corresponds to the (110), (200), and (211) planes of FeCo (PDF 01-075-7975), and sharp peaks of diffraction at 45.9, which corresponds to the (110) planes of Fe (PDF 04-006-4261). Additionally, the sharp diffraction peaks were observed at approximately 40.2°, 47.3°, 52.9, 54.1°, 54.7°, 74.6°, and 79.4 corresponding to the (111), (210), (002), (300), (211), (400), and (302) planes of Fe_2P plane (PDF 00-027-1171). Moreover, Furthermore, a sharp diffraction peak, corresponding to the CoP_2 plane (PDF 00-026-0481), was observed for $P_{0.025}$-FeCo/C and $P_{0.03}$-FeCo/C at approximately 35.7°. The unique electronic structure and suitable electron density of the Metal-P bond provide excellent electrocatalytic performance. Furthermore, sharp diffraction peaks were observed at about 37.4, 39.9, and 43.7 for $P_{0.01}$-FeCo/C, $P_{0.015}$-FeCo/C, and $P_{0.025}$-FeCo/C, corresponding to the (100), (111), and (110) planes of the FexN plane (PDF 04-009-6567, 04-007-3379). Fe-N, as the catalyst's active site, can improve the catalyst's performance [43-44].

Figure 4(b) shows the assessment of the degree of graphitization and defects in all the samples using Raman spectroscopy. A G band, corresponding to the vibrational frequency of the graphite lattice, served to assess the level of graphitization in the material. A high-intensity G band, typically around 1580 cm^{-1}, indicates a high graphitization level. A D band at approximately 1350 cm^{-1} resulted from radiation scattering due to the amorphous state or defects within the material [45-46]. The

ACCEPTED MANUSCRIPT

intensity of the D band reflected the degree of the defects. A stronger D-band signal suggests a higher degree of defects in a material. An I_D/I_G ratio served to compare the extent of graphitization across the different samples. Specifically, the I_D/I_G values of $P_{0.01}$-FeCo/C, $P_{0.015}$-FeCo/C, $P_{0.025}$-FeCo/C, and $P_{0.03}$-FeCo/C were 1.001, 1.008, 1.009, and 1.013, respectively. Heteroatom doping introduces defects in the carbon lattice and exposes edge planes. As the phosphoric acid content increases, the degree of defects increases. ORR activity was generated by activating the π electrons, which was achieved by disrupting the integrity of its π-conjugated structure. Therefore, p doping in sp_2 carbons resulted in defects by breaking the integrity of its π-conjugated structure, thus enhancing the activity of the ORR [47-48].

Figure 5 presents the chemical bonding characteristics of $P_{0.01}$-FeCo/C, $P_{0.015}$-FeCo/C, $P_{0.025}$-FeCo/C, and $P_{0.03}$-FeCo/C, as analyzed by XPS. The binding energies observed in the XPS spectrum were adjusted using the binding energy of C 1s (284.5 eV) used as a reference. Figure 5(a) shows the P 2p XPS spectrum. The characteristic peaks for P $2p_{3/2}$ and P $2p_{1/2}$ in metal phosphides were observed at 128.76 and 129.76 eV, respectively. The spectra of $P_{0.03}$-FeCo/C exhibited a slightly negative shift compared to that of $P_{0.01}$-FeCo/C. The peak around 133.57 eV corresponds to the P–O bond and can be attributed to the phosphate species on the catalyst surface [49-50]. The Fe 2p XPS spectrum (Figure 5(e)) exhibited a spin-orbit doublet. In $P_{0.01}$-FeCo/C, the Fe 2p peaks observed at 732.50, 727.21, 723.35, 719.52, 714.19, 711.18, and 707.70 eV corresponded to satellite peaks, Fe $2p_{1/2}$ of Fe^{3+}, Fe $2p_{1/2}$ of Fe^{2+}, satellite peaks, Fe $2p_{3/2}$ of Fe^{3+}, Fe $2p_{3/2}$ of Fe^{2+}, and Fe-C respectively [50, 51]. The binding energy of Fe $2p_{3/2}$ of Fe^{3+} and Fe^{2+} in $P_{0.03}$-FeCo/C was shifted to higher binding energies compared with that in $P_{0.01}$-FeCo/C, whereas the P $2p_{1/2}$ and $2p_{3/2}$ spectra shift to lower energies. This indicates more positively charged Fe ($Fe^{\delta+}$) and negatively charged P ($P^{\delta-}$) in $P_{0.03}$-

ACCEPTED MANUSCRIPT

FeCo/C than in $P_{0.01}$-FeCo/C. This may benefit the ORR because more positive $Fe^{\delta+}$ and negative $P^{\delta-}$ are favorable to work cooperatively as proton-acceptor centers, respectively [52-54]. The electron donation from the surrounding phosphorus can make $Fe^{\delta+}$ of P-FeCo/C less positive, thereby reducing the binding strength with OH* and showing better catalytic performance and kinetics. The C 1s XPS spectrum (Figure 5(b)) reveals characteristic peaks corresponding to C–C, C–O/C–P, N-C and O–C=O bonds at 284.5, 285.22, 286.01, and 288.36 eV, respectively. The polarity of the C-P bond is opposite to that of the C-N bond. This means that phosphorus-doped carbon materials can generate more defective sites and new active sites that are different from nitrogen-doped carbon materials. Figure 5(c) shows the N 1s spectrum. The detection of N–C and C–P bonds revealed the doping of N and P atoms into the carbon support. The peaks around 401.16, 400.40, 398.72, and 398.07 eV corresponded to graphitic, pyrrolic, metallic, and pyridinic N, respectively. Metal-coordinated nitrogen (Fe-N and Co-N) is crucial for improving the ORR performance of carbon-based catalysts. The O 1s XPS spectrum of $P_{0.01}$-FeCo/C (Figure 5(d)) showed characteristic peaks at 533.82, 532.50, and 531.00 eV, representing O–H/O–C, O–P, and O–M bonds, respectively. Compared to those of $P_{0.01}$-FeCo/C, the O–H/O–C and O–M peaks of $P_{0.03}$-FeCo/C were slightly negative shifted, indicating charge redistribution due to the increased P content. Figure 5(f) shows the Co 2p XPS spectrum. The peaks located at 791.28 and 776.45 eV corresponded to the Co-P bond [50, 55]. The peaks located at 804.89 and 785.68 eV corresponded to the satellite peaks [56]. The peaks located at 796.45 and 781.80 eV corresponded to Co $2p_{1/2}$ and Co $2p_{3/2}$ [57]. The above characterizations prove that we have successfully prepared P, Fe, and Co co-doped carbon matrix catalysts. Heteroatom doping can introduce charge delocalization and asymmetric spin density of carbon atoms, enhancing ORR kinetics.

ACCEPTED MANUSCRIPT

The electrochemically active surface area (ECSA) of an electrode is regarded as an essential factor for ORR efficiency, and it provides a basis for assessing the catalytic sites available for electrochemical reactions. For ECSA measurements, cyclic voltammograms are typically obtained in an O_2-free electrolyte to avoid the influence of ORR currents [58]. Figures 6 (a–d) show the CVs of $P_{0.01}$-FeCo/C, $P_{0.015}$-FeCo/C, $P_{0.025}$-FeCo/C, and $P_{0.03}$-FeCo/C, respectively, measured in 0.1 M KOH electrolyte an Ar-saturated at different various spin speeds. Four electrodes exhibited quasi-rectangular CV curves, which are characteristic of the charge and discharge process of electrostatic double-layer capacitors. The electric double-layer capacitance (C_{dl}) and ECSA calculation equations under the non-Faraday potential window (0.1-0.3 V) [59-60] are as follows [61-63].

$$C_{dl} = j/r \quad (1)$$

$$ECSA = C_{dl}/C_s \quad (2)$$

Here, j corresponds to the current density, Cs represents the specific capacitance, and r corresponds to the scan rate. The C_{dl} linear fitting and ECSA values of $P_{0.01}$-FeCo/C, $P_{0.015}$-FeCo/C, $P_{0.025}$-FeCo/C, and $P_{0.03}$-FeCo/C are shown in Figures 6 (e and f). The C_{dl} values of $P_{0.01}$-FeCo/C, $P_{0.015}$-FeCo/C, $P_{0.025}$-FeCo/C, and $P_{0.03}$-FeCo/C electrodes were 36.5, 56.6, 68.4, and 49.8 mF cm^{-2}, respectively. The ECSA values were 1422.3, 1616.9, 1954.3, and 1043.1 cm^2, respectively. The results showed that $P_{0.025}$-FeCo/C had the highest ECSA, demonstrating that it had a greater number of electrochemically active sites than the other electrodes [64]. This was attributed to the P-doping, which introduced defects into the carbon lattice, exposed edge planes, and enhanced the available active sites. This tubular offered numerous active sites and superior electron transport pathways through its unique channels and cavities.

ACCEPTED MANUSCRIPT

As shown in Figure 7 and S1, LSV tests were conducted to investigate the ORR activities of the catalysts. $P_{0.025}$-FeCo/C exhibited an excellent limited current density of -3.98 mA/cm^2, a half-wave potential ($E_{1/2}$) of ~ 0.84 V, and an onset potential (E_{onset}) of ~ 0.94 V, compared with the $P_{0.01}$-FeCo/C, $P_{0.015}$-FeCo/C, and $P_{0.03}$-FeCo/C electrodes. ($P_{0.01}$-FeCo/C: limited current density = -3.27 mA/cm^2, $E_{1/2}$ = 0.79 V, and E_{onset} = 0.90 V; $P_{0.015}$-FeCo/C: limited current density of -3.40 mA/cm^2, $E_{1/2}$ = 0.82 V, and E_{onset} = 0.92 V; $P_{0.03}$-FeCo/C: limited current density = -2.95 mA/cm^2, $E_{1/2}$ = 0.78 V, and E_{onset} = 0.89 V). Compared with other published papers, $P_{0.025}$-FeCo/C sample outperformed the E_{onset} and $E_{1/2}$ (Table 1) [65-72]. To evaluate the ORR performance of these catalysts compared with Pt/C. For comparison, the E_{onset} and $E_{1/2}$ values of Pt/C were 0.95 and 0.86 V under the same condition, respectively. $P_{0.025}$-FeCo/C is comparable to that of the benchmark Pt/C catalyst (Table 2). We demonstrated that $P_{0.025}$-FeCo/C exhibited good catalytic activity. This trend indicates that P doping can enhance the ORR activity by introducing defects to promote the generation of π electrons. Because of its unique channels and cavities, the tubular structure provides superior electron-transfer paths and numerous active sites. The unique electronic structure and suitable electron density of TMPs provide them with excellent electrocatalytic performance. However, compared with the other samples, the ORR performance of $P_{0.03}$-FeCo/C dropped sharply. This was attributed to the excessive phosphoric acid content, which destroyed the nanotube structure, reduced the electrical conductivity of the carbon support, and affected the transmission efficiency of electrons in the catalyst, ultimately resulting in reduced catalytic performance.

To evaluate the electrocatalytic stability of the electrodes, an accelerated durability test was performed. After completion of the ADT, the LSV analyses were conducted again at 1600 rpm. As shown in Figure 8 and S2, $P_{0.025}$-FeCo/C showed

ACCEPTED MANUSCRIPT

excellent long-term stability in terms of ORR activity among all samples, with the potential degradation evaluated at $E_{1/2}$ ($\Delta E_{1/2}$) being 3.3 mV (FeCo/C: $\Delta E_{1/2}$ of 24.6 mV; $P_{0.01}$-FeCo/C: $\Delta E_{1/2}$ of 10.7 mV; $P_{0.015}$-FeCo/C: $\Delta E1_{/2}$ of 8.6 mV; $P_{0.03}$-FeCo/C: $\Delta E_{1/2}$ of 11.8 mV). Furthermore, we evaluated the electrocatalytic stability of $P_{0.025}$-Fe/C and $P_{0.025}$-Co/C (Figure S2 (b) and (c)). The results showed $\Delta E_{1/2}$ values of approximately 11.0 mV and 5.5 mV, respectively. More importantly, $P_{0.025}$-Fe/C, $P_{0.025}$-Co/C, and P_x-FeCo/C exhibit better potential degradation evaluated than Pt/C catalyst ($\Delta E_{1/2}$ of 16.7 mV. Figure 8 (e). Table 2). These findings suggest that metal phosphides play a crucial role in enhancing the electrochemical stability of carbon-supported catalysts in alkaline environments. Incorporating P helps prevent dissolution or structural degradation, maintaining the structural integrity of the catalyst over prolonged use. Co–P bonds exhibit higher binding energies and more substantial chemical stability than Fe–P bonds. This stronger bond reduces the dissociation or decomposition of the catalyst structure during the reaction, further enhancing the material's long-term stability. However, excessive P-doping destroys the carbon nanotube structure, blocks the active sites on the carbon nanocarriers, and reduces the stability of the catalyst.

The durability and methanol poisoning resistance of non-precious metal catalysts in alkaline solutions is key for practical applications. The stability of the catalysts in oxygen-saturated electrolytes was evaluated by chronoamperometric curves (i-t curves) (Figure 9). After running in 0.1 M KOH for 10,000 seconds, the current density of catalyst $P_{0.025}$-FeCo/C remained at 86% of the initial value, which was higher than 72% of the commercial Pt/C catalyst, indicating that $P_{0.025}$-FeCo/C has better long-term stability. In addition, Pt/C electrodes are easily deactivated in the presence of methanol. To study the performance of the catalyst against the cross-effect of methanol, 10 mL of methanol was added to the electrolyte at 300 seconds (total electrolyte volume

ACCEPTED MANUSCRIPT

was 100 mL) in the experiment. The results showed that the oxygen reduction reaction current density of Pt/C decreased significantly compared with catalyst $P_{0.025}$-FeCo/C, showing poor methanol tolerance. Overall, $P_{0.025}$-FeCo/C exhibits excellent stability and methanol poisoning resistance in alkaline media. These characteristics make it a promising non-precious metal electrocatalyst, providing a vital research basis for practical applications.

4. Conclusion

In this research, we prepared P-doped bimetallic FeCo catalysts on carbon matrix via electrospinning, in situ growth, and pyrolysis. Carbon nanotubes grew directionally around CNF from the MOFs, and the porous structure offered additional space for their formation. The $P_{0.025}$-FeCo/C catalyst demonstrated outstanding ORR activity, including an ECSA of 1954.3 cm^2, a limited current density of -3.98 mA/cm^2, an $E_{1/2}$ of ~ 0.84 V, and an E_{onset} of ~ 0.94 V. After 5000 cycles, the $P_{0.025}$-FeCo/C catalyst demonstrated remarkable enduring stability. These performance improvements are due to the following: First, P doping introduces defects into the carbon lattice, which disrupt the π-conjugated structure and promote the generation of π electrons to enhance the ORR activity. Secondly, the unique electronic structure and suitable electron density of TMPs provide excellent electrocatalytic performance. Furthermore, they resist dissolution or collapse in alkaline environments and maintain good chemical and electrochemical stability during long-term cycling. Finally, the tubular structure within the carbon carrier provides numerous active sites and superior electron transport pathways owing to its unique channels and cavities, which enhance both the durability and activity of the catalyst.

ACCEPTED MANUSCRIPT

Acknowledgements

This work is supported by the Basic Science Research Program through the National Research Foundation of Korea (NRF) funded by the Ministry of Education (NRF-2021R1A6A1A03039981) and National Research Foundation of Korea (NRF) grant funded by the Korea government (MSIT) (RS-2023-00209244).

Disclosure statement

The authors report there are no competing interests to declare.

Data availability statement

Data will be made available on request.

References

[1] Wuebbles D J, Jain, A K. Concerns about climate change and the role of fossil fuel use. Fuel Process. Technol. 2001;71(1-3):99–119.

[2] Dincer I, Renewable energy and sustainable development: a crucial review. Renew. Sust. Energ. Rev. 2000;4(2):157–175.

[3] Bilgen S. Structure and environmental impact of global energy consumption. Renew. Sust. Energ. Rev. 2014;38:892–902.

[4] Dudin M N, Frolova E E, Protopopova O V, et al. Study of innovative technologies in the energy industry: nontraditional and renewable energy sources. Entrepreneurship. Sustain. 2019;6:1704–1713.

[5] Lee, J M, Han H S, Jin S, et al. A review on recent progress in the aspect of stability of oxygen reduction electrocatalysts for proton-exchange membrane fuel cell: Quantum Mechanics and Experimental Approaches. Energy Technol. 2019;7(9):1900312.

ACCEPTED MANUSCRIPT

[6] Chen X Q, Ali I, Song L, et al. A review on recent advancement of nano-structured-fiber-based metal-air batteries and future perspective. Renew. Sust. Energ. Rev. 2020;134:110085.

[7] Ren X M, Zhang S S, Tran D T, et al. Oxygen reduction reaction catalyst on lithium/air battery discharge performance. J. Mater. Chem. 2011;21:10118–10125.

[8] Bezerra L S, Maia G. Developing efficient catalysts for the OER and ORR using a combination of Co, Ni, and Pt oxides along with graphene nanoribbons and $NiCo_2O_4$. J. Mater. Chem. A. 2020;8:17691–17705.

[9] Shi Z S, Yang W Q, Gu Y T, et al. Metal–nitrogen–doped carbon materials as highly efficient catalysts: progress and rational design. Adv. Sci. 2020;7(15):2001069.

[10] Osgood H, Devaguptapu S V, Xu H, et al. Transition metal (Fe, Co, Ni, and Mn) oxides for oxygen reduction and evolution bifunctional catalysts in alkaline media. Nano Today. 2016;11(5):601–625.

[11] Liu X, Zhang G Y, Wang L, et al. Structural design strategy and active site regulation of high-efficient bifunctional oxygen reaction electrocatalysts for Zn–air battery. Small. 2021;17(48):2006766.

[12] Huang X X, Shen T, Zhang T, et al. Efficient oxygen reduction catalysts of porous carbon nanostructures decorated with transition metal species. Adv. Energy Mater. 2019;10(11):1900375.

[13] Huang Z F, Wang J, Peng, Y C, et al. Design of efficient bifunctional oxygen reduction/evolution electrocatalyst: recent advances and perspectives. Adv. Energy Mater. 2017;7(23):1700544.

[14] Cheng F Y, Chen, J. Metal–air batteries: from oxygen reduction

ACCEPTED MANUSCRIPT

electrochemistry to cathode catalysts. Chem. Soc. Rev. 2012;41:2172–2192.

[15]Chen Y J, Ji S F, Chen C, et al. Single-atom catalysts: synthetic strategies and electrochemical applications. Joule. 2018;2(7):1242–1264.

[16]Guo Y N, Park T, Yi, J W, et al. Nanoarchitectonics for transition-metal-sulfide-based electrocatalysts for water splitting. Adv. Mater. 2019;31(17):1807134.

[17]Attarzadeh N, Nuggehalli R, Ramana C V. Application of transition metal phosphides to electrocatalysis: an overview. JOM. 2022;74:381–395.

[18]Su J Z, Zhou J L, Wang L, et al. Synthesis and application of transition metal phosphides as electrocatalyst for water splitting. Sci. Bull. 2017;62(9):633–644.

[19]Li S H, Qi M Y, Tang Z R, et al. Nanostructured metal phosphides: from controllable synthesis to sustainable catalysis. Chem. Soc. Rev. 2021;50:7539–7586.

[20]Subbiah T, Bhat G S, Tock R, et al. Electrospinning of nanofibers. J. Appl. Polym. Sci. 2005;96(2):557–569.

[21]Yan Y H, Liu X Y, Yan J, et al. Electrospun nanofibers for new generation flexible energy storage. Energy Environ. Mater. 2020;4(4):502–521.

[22]Jiao L, Seow J Y R, Skinner W S, et al. Metal–organic frameworks: Structures and functional applications. Mater. Today. 2019;27:43–68.

[23]Xia Q, Wang H, Huang B B, et al. State-of-the-art advances and challenges of iron-based metal organic frameworks from attractive features, synthesis to multifunctional applications. Small. 2018;15(12):1803088.

[24]Aijaz A, Xu Q. Catalysis with metal nanoparticles immobilized within the pores of metal–organic frameworks. J. Phys. Chem. Lett. 2014;5(8):1400–1411.

[25]Meng J S, Niu C J, Xu L H, et al. General oriented formation of carbon

ACCEPTED MANUSCRIPT

nanotubes from metal–organic frameworks. J. Am. Chem. Soc. 2017;139(24):8212–8221.

[26]Arbulu R C, Jiang Y B, Peterson E J, et al. Metal–organic framework (MOF) nanorods, nanotubes, and nanowires. Angew. Chem.-Int. Edit. 2018;57(20):5813–5817.

[27]Chen X C, Lukaszczuk P, Tripisciano C Rümmeli, et al. Enhancement of the structure stability of MOF-5 confined to multi-walled carbon nanotubes. Phys. Status Solidi B-Basic Res. 2010;247(11-12):2664–2668.

[28]Zou L L, Hou C C, Liu Z, et al. Superlong single-crystal metal–organic framework nanotubes. J. Am. Chem. Soc. 2018;140(5):15393–15401.

[29]Zhang Y Z, Huang Q H, Liu J W, et al. Recent advances in Fe-based metal-organic framework derivatives for battery applications. Sustainable Energy Fuels. 2022;6:2665–2691.

[30]Dhakshinamoorthy A, Alvaro M, Garcia H. Metal–organic frameworks as heterogeneous catalysts for oxidation reactions. Catal. Sci. Technol. 2011;1:856–867.

[31]Corma A, García H, Llabrés i Xamena F X. Engineering metal organic frameworks for heterogeneous catalysis. Chem. Rev. 2010;110(8):4606–4655.

[32]Yang L J, Fang S Z, Xu G C, et al. Electrospun MOF-based FeCo nanoparticles embedded in nitrogen-doped mesoporous carbon nanofibers as an efficient bifunctional catalyst for oxygen reduction and oxygen Evolution reactions in zinc-air batteries. ACS Sustainable Chem. Eng. 2019;7(5):5462–5475.

[33]Lei Y P, Wang Q C, Peng S, et al. Electrospun inorganic nanofibers for oxygen electrocatalysis: design, fabrication, and progress. Adv. Energy Mater. 2020;10(45):1902115.

ACCEPTED MANUSCRIPT

[34]Zhang X, Wang L. Research progress of carbon nanofiber-based precious-metal-free oxygen reaction catalysts synthesized by electrospinning for Zn-Air batteries. J. Power Sources. 2021;507:230280.

[35]Zhang Y G, Zhang Y F, Wang X F, et al. Ultrahigh metal–organic framework loading and flexible nanofibrous membranes for efficient CO_2 capture with long-term, ultrastable recyclability. ACS Appl. Mater. Interfaces. 2018;10(40):34802–34810.

[36]Li L, Zhang X, -Liu S A, et al. One-step hydrothermal synthesis of $NiCo_2S_4$ loaded on electrospun carbon nanofibers as an efficient counter electrode for dye-sensitized solar cells. Sol. Energy. 2020;202(15):358–364.

[37]Zhao Z H, Liu M J, Zhou K, et al. Zr-based metal−organic frameworks with phosphoric acids for the photo-oxidation of sulfides. Int. J. Mol. Sci. 2022;23(24):16121.

[38]Zhao C X, Jiao Y, Hu F, et al. Green synthesis of carbon dots from pork and application as nanosensors for uric acid detection. Acta A Mol. Biomol. Spectrosc. 2018;190:360–367.

[39]Sun S F, Zhou X, Cong B W, et al. Tailoring the d-band centers endows $(NixFe1-x)_2P$ nanosheets with efficient oxygen evolution catalysis. ACS Catal. 2020;10(16):9086–9097.

[40]Wan J W, Zhao Z H, Shang H, et al. In situ phosphatizing of triphenylphosphine encapsulated within metal-organic frameworks to design atomic Co_1-P_1N_3 interfacial structure for promoting catalytic performance. J. Am. Chem. Soc. 2020;142(18):8431–8439.

[41]Shinde S S, Jung J Y, Wagh N K, et al. Ampere-hour-scale zinc–air pouch cells. Nat. Energy. 2021;6:592–604.

ACCEPTED MANUSCRIPT

[42]Lin Y X, Yang L, Zhang Y K, et al. Defective carbon–CoP nanoparticles hybrids with interfacial charges polarization for efficient bifunctional oxygen electrocatalysis. Adv. Energy Mater. 2018;8(18):1703623.

[43]Niu H J, Lin, S Y, Chen Y P, et al. Hydrogel derived FeCo/FeCoP embedded in N, P-codoped 3D porous carbon framework as a highly efficient electrocatalyst for oxygen reduction reaction. Appl. Surf. Sci. 2021;536:147950.

[44]Liu Z, Zheng P, Liu L, et al. MOF-derived FeCo carbon nanomaterials with abundant oxygen vacancies as highly efficient peroxymonosulfate catalyst for ciprofloxacin degradation. J. Environ. Chem. Eng. 2023;11(5):110603.

[45]Ferrari A C, Basko D M. Raman spectroscopy as a versatile tool for studying the properties of graphene. Nat. Nanotechnol. 2013;8:235–246.

[46]Ćirić-Marjanović G, Pašti I, Gavrilov N, et al. Carbonised polyaniline and polypyrrole: towards advanced nitrogen-containing carbon materials. Chem. Pap. 2013;67(8):781–813.

[47]Zhao Y, Yang L J, Chen S, et al. Can boron and nitrogen co–doping improve oxygen reduction reaction activity of carbon nanotubes. J. Am. Chem. Soc. 2013;135(4):1201–1204.

[48]Behan J A, Mates–Torres E, Stamatin S N, et al. Untangling cooperative effects of pyridinic and graphitic nitrogen sites at metal-free N doped carbon electrocatalysts for the oxygen reduction reaction. Small. 2019;15(48):1902081.

[49]Luo L, Li W J, Wang Y W, et al. Se and Fe co-doping in $Ni_2P/Ni_{12}P_5$/NF: Highly active and ultra-long stability of the oxygen evolution reaction. Appl. Surf. Sci. 2022;606:154950.

[50]Liu Y L, Ge P J, Li Y F, et al. Prussian blue analogues derived Fe-NiCoP reveals the cooperation of Fe doping and phosphating for enhancing OER

ACCEPTED MANUSCRIPT

activity. Appl. Surf. Sci. 2023;615:156378.

[51]Chen W D, Yu H P, Chang S M, et al. Wheat straw as carbon source to prepare $FeCoP_2$/N, P Dual-Doped carbon matrix as bifunctional catalyst for application in rechargeable Zinc-air and Aluminum-air batteries. Appl. Surf. Sci. 2022;573(30):151486.

[52]Yao Y D, Mahmood N, Pan L, et al. Iron phosphide encapsulated in P-doped graphitic carbon as efficient and stable electrocatalyst for hydrogen and oxygen evolution reactions. Nanoscale. 2018;10:21327–21334.

[53]Zhang T, Yang T X, Li B, et al. MOF-derived formation of ultrafine FeP nanoparticles confined by N/P Co-doped carbon as an efficient and stable electrocatalyst for hydrogen evolution reaction. Appl. Surf. Sci. 2022;597(30):153662.

[54]Wang Y, Zhang J R, Wang X W, et al. Bimetal-organic framework-derived nanorod-like $FexNi_{1-x}$@C, P composites for electrochemical hydrogen evolution. J. Alloy. Compd. 2023;931(10):167511.

[55]Song S Y, Guo M J, Zhang S, et al. Plasma-assisted synthesis of hierarchical $NiCo_xP_y$ nanosheets as robust and stable electrocatalyst for hydrogen evolution reaction in both acidic and alkaline media. Electrochim. Acta. 2020;331:135431.

[56]Tang F, Zhao Y W, Ge Y, et al. Synergistic effect of Mn doping and hollow structure boosting Mn-CoP/Co_2P nanotubes as efficient bifunctional electrocatalyst for overall water splitting. J. Colloid Interface Sci. 2022;628(B):524–533.

[57]Zhang, S S, Guo M J, Song S Y, et al. Hierarchical Mo-doped $CoP_{(3)}$ interconnected nanosheet arrays on carbon cloth as an efficient bifunctional

ACCEPTED MANUSCRIPT

electrocatalyst for water splitting in an alkaline electrolyte. Dalton Trans. 2020;49:5563–5572.

[58]Lee J S, Rajan H, Christy M, et al. Optimization of active sites by sulfurization of the core–shell ZIF 67@ZIF 8 for rapid oxygen reduction kinetics in acidic media. Int. J. Hydrog. Energy. 2021;46(18):10739–10748.

[59]Sirisomboonchai S, Li S S, Yoshida A, et al. Terephthalic acid induced binder-free NiCoP-carbon nanocomposite for highly efficient electrocatalysis of hydrogen evolution reaction. Catal. Sci. Technol. 2019;9:4651–658.

[60]Yilmaz G, Tan C F, Hong M H, et al. Functional defective metal-organic coordinated network of mesostructured nanoframes for enhanced electrocatalysis. Adv. Funct. Mater. 2018;28(12):1704177.

[61]Zhou Z H, Zaman W Q, Sun W, et al. Cultivating crystal lattice distortion in IrO_2 via coupling with MnO_2 to boost the oxygen evolution reaction with high intrinsic activity. Chem. Commun. 2018;54:4959–962.

[62]Pu Z H, Cheng R L, Zhao J H, et al. Anion–modulated platinum for high-erformance multifunctional electrocatalysis toward HER, HOR, and ORR. iScience. 2020;23(12):101793.

[63]Ong A L, Inglis K K, Whelligan D K, et al. Effect of cationic molecules on the oxygen reduction reaction on fuel cell grade Pt/C (20 wt%) catalyst in potassium hydroxide. Phys. Chem. Chem. Phys. 2015;17:12135–2145.

[64]An G H, Lee E H, Ahn H J. Ruthenium and ruthenium oxide nanofiber supports for enhanced activity of platinum electrocatalysts in the methanol oxidation reaction. Phys. Chem. Chem. Phys. 2016;18:14859–14866.

[65]Liang Z, Fan X, Lei H, et al. Cobalt–nitrogen-doped helical carbonaceous nanotubes as a class of efficient electrocatalysts for the oxygen reduction

ACCEPTED MANUSCRIPT

reaction. Angew. Chem. Int. Ed. 2018;130:13371–13375.

[66]Chang H, Min W, Han C, et al. N- and P, N-doped graphene as highly active catalysts for oxygen reduction reactions in acidic media. J. Mater. Chem. A. 2013;1:3694–3699.

[67]Sadighi Z, Liu J, Zhao L, et al. Metallic MoS_2 nanosheets: Multifunctional electrocatalyst for the ORR, OER and Li–O_2 batteries. Nanoscale. 2018;10:22549–22559.

[68]Wu Y, Chen Y, Wang H, et al. Efficient ORR electrocatalytic activity of peanut shell-based graphitic carbon microstructures. J. Mater. Chem. A. 2018;6:12018–12028.

[69]Sheng K, Yi Q, Chen A L, et al. CoNi nanoparticles supported on N-doped bifunctional hollow carbon composites as high-performance ORR/OER catalysts for rechargeable Zn–air batteries. ACS Appl. Mater. Interfaces. 2021;13:45394–45405.

[70]Jiang H, Wang Y, Hao J, et al. N and P co-functionalized three-dimensional porous carbon networks as efficient metal-free electrocatalysts for oxygen reduction reaction. Carbon. 2017;122:64–73.

[71]Tang Y, Liu R, Liu S, et al. Cobalt and nitrogen codoped ultrathin porous carbon nanosheets as bifunctional electrocatalysts for oxygen reduction and evolution. Carbon. 2019;141:704–711.

[72]Mo J, Müller T, Oliveira J C A, et al. Iron-Catalyzed C-H Activation with Propargyl Acetates: Mechanistic Insights into Iron (II) by Experiment, Kinetics, Mössbauer Spectroscopy, and Computation. Angew. Chem. Int. Ed. 2019;58:12874–12878.

ACCEPTED MANUSCRIPT

Tables and captions

Table 1. Compared to other published papers, the value of E_{onset} and $E_{1/2}$.

Catalysts	E_{onset} (V)	$E_{1/2}$ (V)
CCNTs-Co-800	0.90	0.84
Co/FN-C	0.917	0.753
1T-MoS_2	0.90	0.81
CoOP@bio-C	0.91	0.81
CoNi/NTUC	0.90	0.84
NPCN-900	0.92	0.78
Co–N–PCN	0.90	0.82
$Pt_{3.5\%}$Ni PF	0.92	0.80
$P_{0.025}$-FeCo/C (this paper)	0.94	0.84

Table 2. Comparing all samples, the value of E_{onset}, $E_{1/2}$, Limited current density, and $\Delta E_{1/2}$.

Catalysts	E_{onset} (V)	$E_{1/2}$ (V)	Limited current density	$\Delta E_{1/2}$(mV)
$P_{0.01}$-FeCo/C	0.90	0.79	-3.27	10.7
$P_{0.015}$-FeCo/C	0.92	0.82	-3.40	8.6
$P_{0.025}$-FeCo/C	0.94	0.84	-3.98	3.3
$P_{0.03}$-FeCo/C	0.89	0.78	-2.95	11.8
Pt/C	0.95	0.86	-3.95	16.7

ACCEPTED MANUSCRIPT

Figures and captions

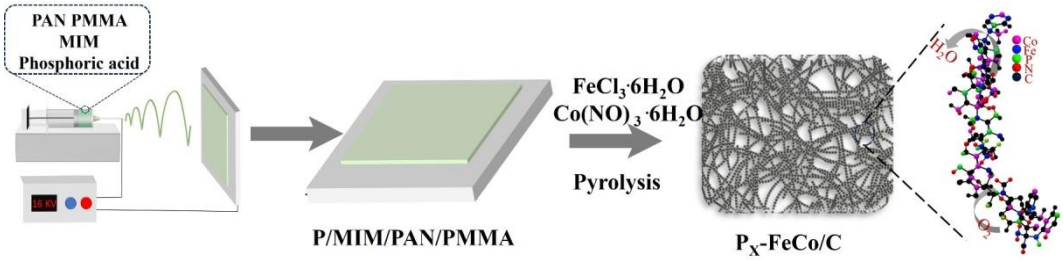

Figure 1. Illustration of the fabrication process of P_x-FeCo/C.

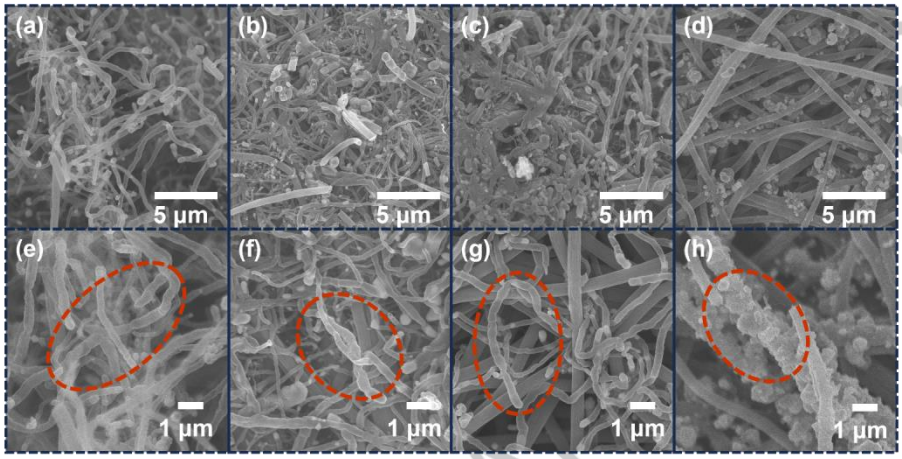

Figure 2. FESEM images of (a, e) $P_{0.01}$-FeCo/C, (b, f) $P_{0.015}$-FeCo/C, (c, g) $P_{0.025}$-FeCo/C, and (d, h) $P_{0.03}$-FeCo/C.

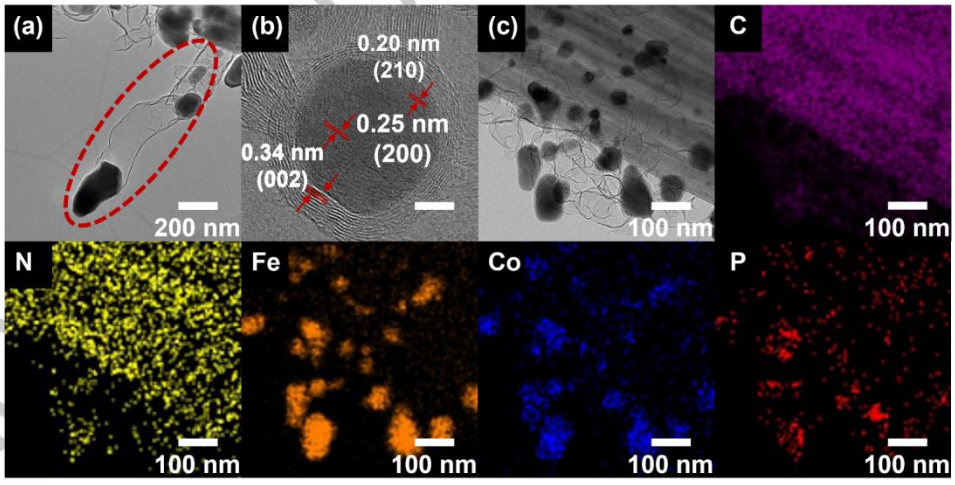

Figure 3. (a) Low- and (b) high-resolution TEM images and (c) EDS mapping of C, N, Fe, Co, and P of $P_{0.025}$-FeCo/C.

ACCEPTED MANUSCRIPT

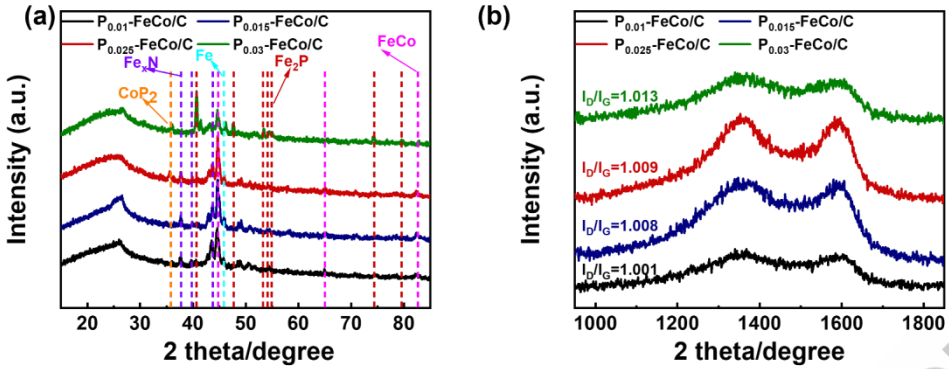

Figure 4. (a) XRD and (b) Raman spectra I_D/I_G ratio of $P_{0.01}$-FeCo/C, $P_{0.015}$-FeCo/C, $P_{0.025}$-FeCo/C, and $P_{0.03}$-FeCo/C.

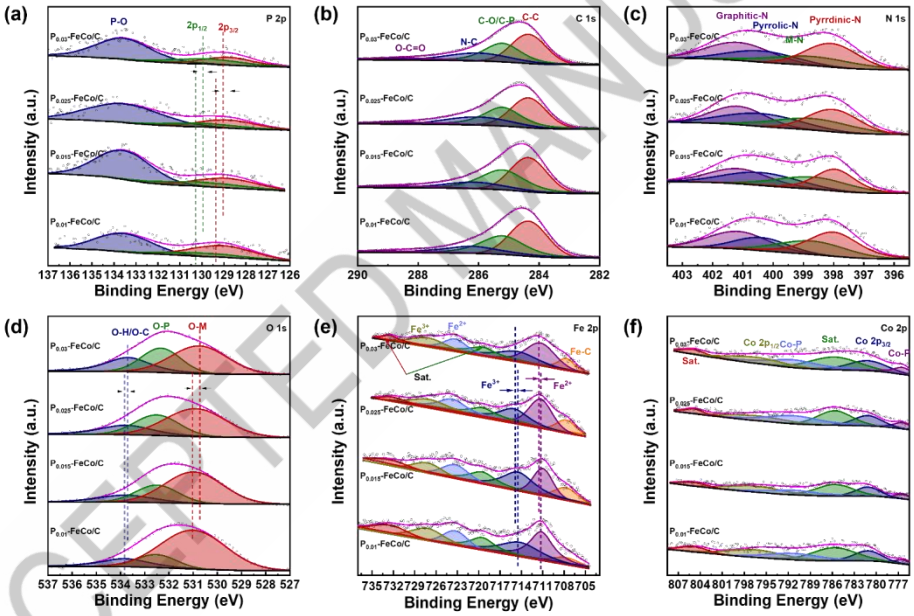

Figure 5. XPS spectrum of $P_{0.01}$-FeCo/C, $P_{0.015}$-FeCo/C, $P_{0.025}$-FeCo/C, $P_{0.03}$-FeCo/C: (a) P 2p, (b) C 1s, (c) N 1s and (d) O 1s (e) Fe 2p, and (f) Co 2p.

ACCEPTED MANUSCRIPT

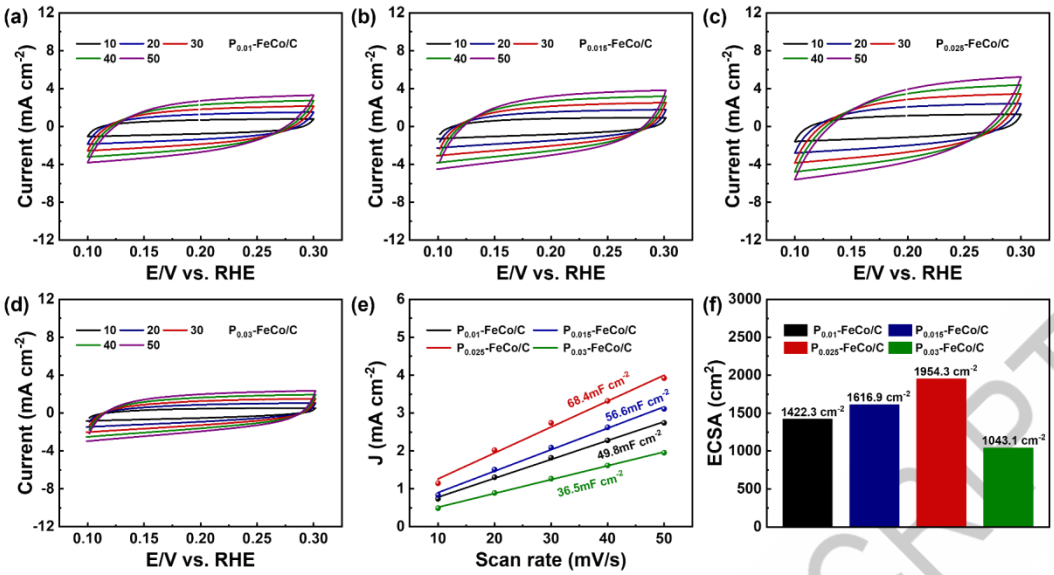

Figure 6. Cyclic voltammetry curves of (a) $P_{0.01}$-FeCo/C, (b) $P_{0.015}$-FeCo/C, (c) $P_{0.025}$-FeCo/C, and (d) $P_{0.03}$-FeCo/C at different scan rates of 10–50 mV s^{-1} in Ar-saturated 0.1 M KOH electrolyte. (e) C_{dl} linear fitting and (f) ECSA values of $P_{0.01}$-FeCo/C, $P_{0.015}$-FeCo/C, $P_{0.025}$-FeCo/C, and $P_{0.03}$-FeCo/C.

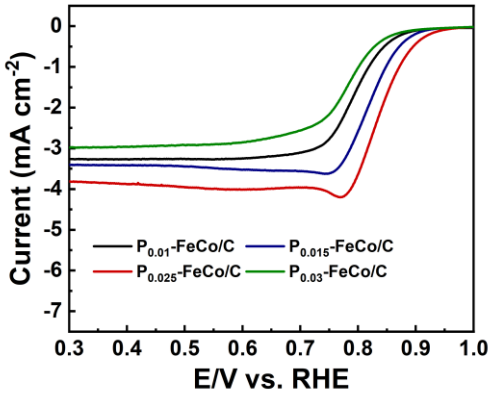

Figure 7. LSV curves of $P_{0.01}$-FeCo/C, $P_{0.015}$-FeCo/C, $P_{0.025}$-FeCo/C, and $P_{0.03}$-FeCo/C.

ACCEPTED MANUSCRIPT

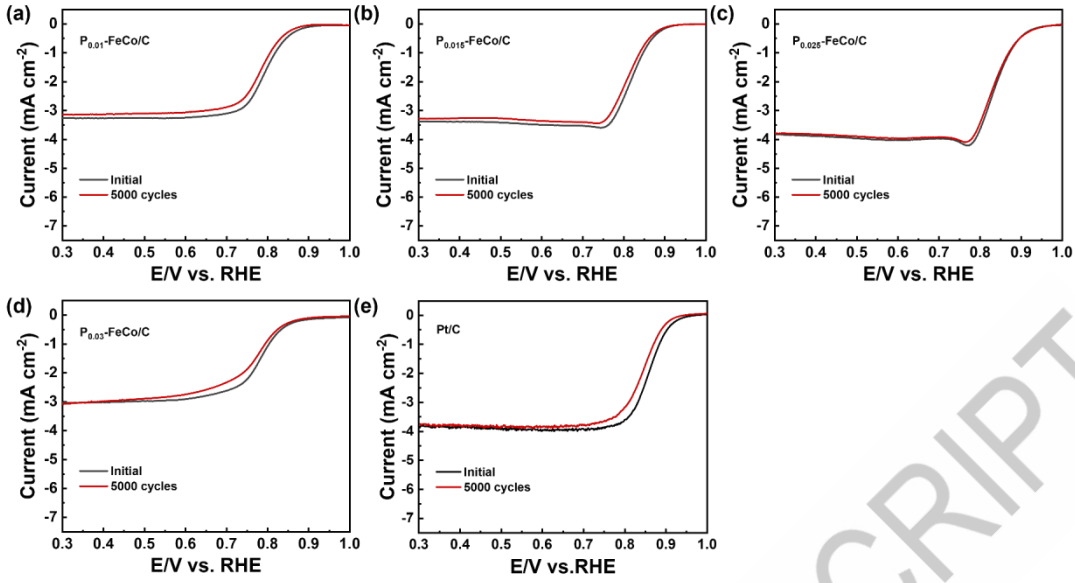

Figure 8. LSV curves of (a) $P_{0.01}$-FeCo/C, (b) $P_{0.015}$-FeCo/C, (c) $P_{0.025}$-FeCo/C, (d) $P_{0.03}$-FeCo/C and (e) Pt/C before and after ADT.

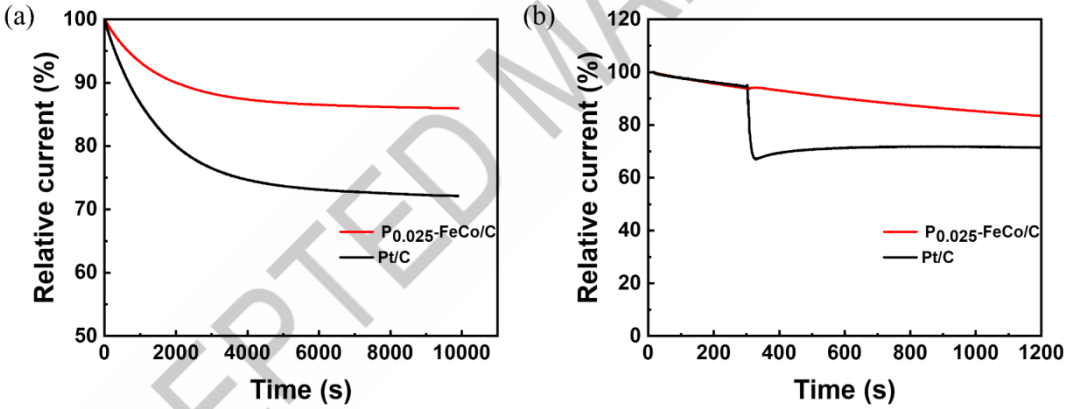

Figure 9. (a) The methanol crossover chronoamperometric curves and chronoamperometric response for ORR of $P_{0.025}$-FeCo/C, and Pt/C in 0.1 M KOH solution at a rotation rate of 1600 rpm.

Statement of Novelty

ACCEPTED MANUSCRIPT

Effect of P doped bimetallic FeCo catalysts on carbon matrix for oxygen reduction in alkaline media

Yuqi Ma, and Hyo-Jin Ahn*

The $P_{0.025}$-FeCo/C catalyst exhibits excellent ORR activity and significant long-lasting stability. It is expected to become a non-noble metal catalyst that promotes oxygen reduction reaction.

ACCEPTED MANUSCRIPT

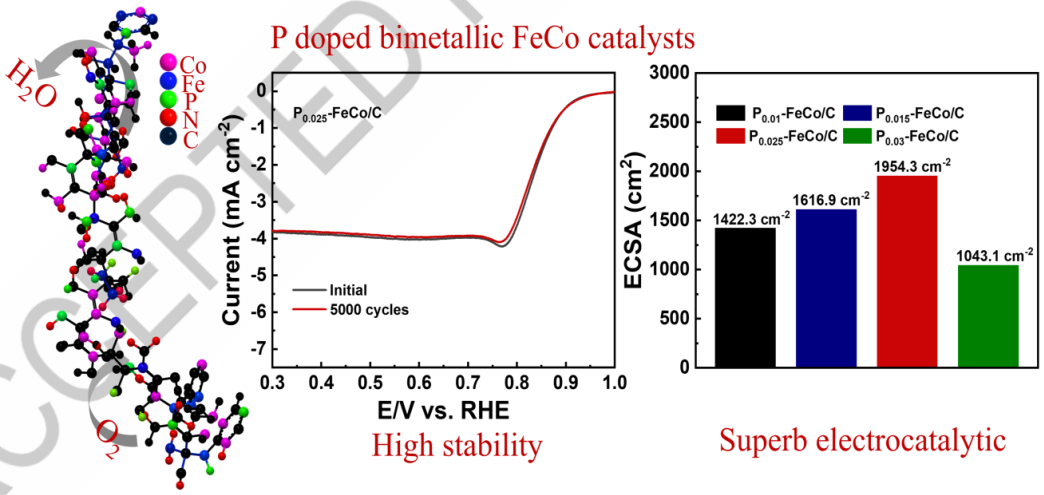

Graphical abstract

Effect of P doped bimetallic FeCo catalysts on carbon matrix for oxygen reduction in alkaline media

Yuqi Ma, and Hyo-Jin Ahn*

Department of Materials Science and Engineering, Seoul National University of Science and Technology, Seoul 01811, Korea

*Corresponding author Tel.: +82-2-970-6622

Email address: hjahn@seoultech.ac.kr (H.-J. Ahn)

yqma@seoultech.ac.kr (Yuqi Ma)

ACCEPTED MANUSCRIPT

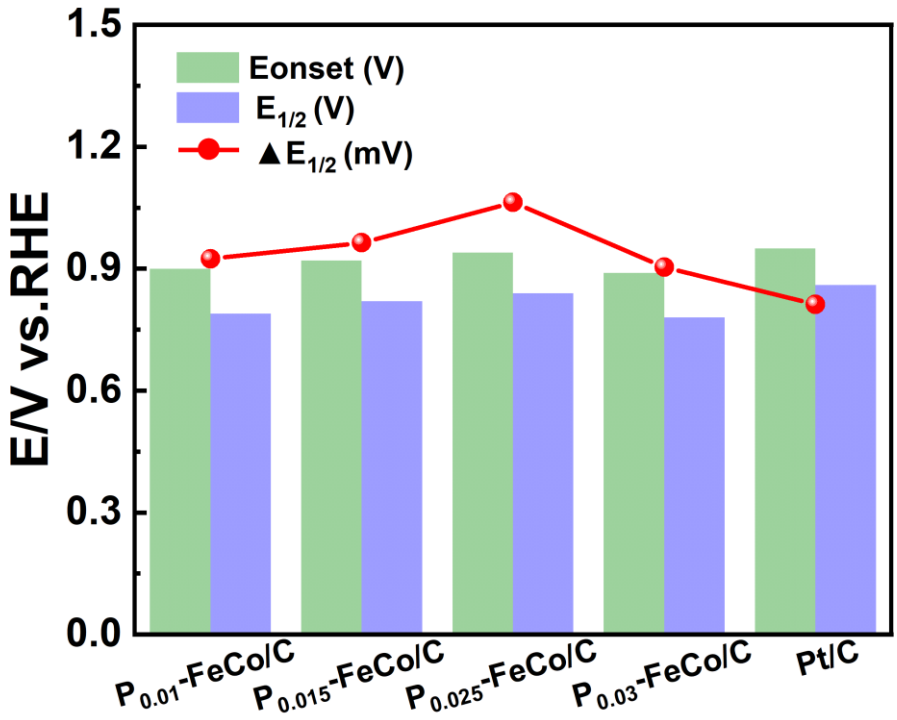

Figure S1. Comparing $P_{0.01}$-FeCo/C、$P_{0.015}$-FeCo/C、$P_{0.025}$-FeCo/C, $P_{0.03}$-FeCo/C, and Pt/C, the value of E_{onset}, $E_{1/2}$, and $\Delta E_{1/2}$

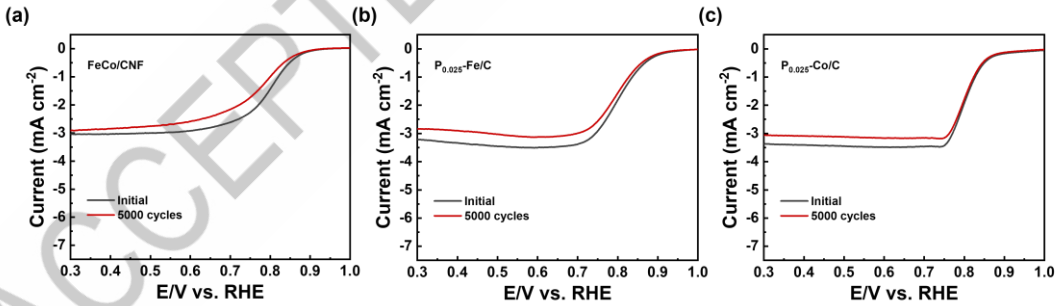

Figure S2. LSV curves of (a) FeCo/C, (b) $P_{0.025}$-Fe/C, and (c) $P_{0.025}$-Co/C before and after ADT.

ACCEPTED M